Home   Search   Collections   Journals   About   Contact us   My IOPscience

Structural study of a sol–gel derived novel solid oxide fuel cell perovskite:

$(La_{1-x}Sr_x)(Cr_{0.85}Fe_{0.05}Co_{0.05}Ni_{0.05})O_{3-\delta}$

Structural study of a sol–gel derived novel solid oxide fuel cell perovskite: $(La_{1-x}Sr_x)(Cr_{0.85}Fe_{0.05}Co_{0.05}Ni_{0.05})O_{3-\delta}$

Ravindra K Gupta and Chin Myung Whang[1]

School of Materials Science and Engineering, Inha University, #253 Yonghyun-dong, Nam-ku, Incheon 402-751, Korea

E-mail: cmwhang@inha.ac.kr

Abstract

The effect of composition on the structure of the new solid oxide fuel cell (SOFC) perovskite $(La_{1-x}Sr_x)(Cr_{0.85}Fe_{0.05}Co_{0.05}Ni_{0.05})O_{3-\delta}$ is studied using x-ray diffractometry, pycnometry, and Fourier-transform infrared and Raman spectroscopy. Samples were synthesized using the Pechini method via doping the La site with Sr^{2+}, to a composition with $x = 0$–0.4 mole fraction, and at the Cr site with 0.05 mol of Co^{2+}, Fe^{2+} and Ni^{2+}, and the structural results were compared with those for orthorhombic $LaCrO_3$. The samples were orthorhombic perovskite of the *Pnma* space group. A second phase, monoclinic $SrCrO_4$, was also observed, whose content increased linearly with increasing x. A large decrease in the lattice and hence volume was observed for the sample with $x = 0.1$, which was accompanied by a sharp decrease in the Cr−O bond length, tilt angle and crystallite size. The structural parameters were almost invariant for $x = 0.1$–0.4, probably due to an increase in content of the high valence cations of smaller ionic radii, as suggested by an increase in the intensity of the defect band (~ 515 cm^{-1}, IR). The octahedral CrO_6 stretching, bending and tilting modes were found shifted accordingly. A mechanism employing a partial-charge model was proposed to explain the results.

(Some figures in this article are in colour only in the electronic version)

1. Introduction

Owing to excellent oxidation, sulfidation and carburization resistances; stability in terms of dimension, microstructure, chemistry and phase; high electronic and thermal conductivity; and comparable coefficient of thermal expansion (CTE) to the adjacent components, Sr^{2+} doped

---

[1] Author to whom any correspondence should be addressed.

LaCrO$_3$ (LSC) perovskite has been extensively applied as an inter-connector coating material, along with its application as cathode and anode in solid oxide fuel cells (SOFCs) operating at 1000 °C. In order to improve its air sinterability and electrical conductivity at intermediate temperature (IT, =500–700 °C) of operation, several approaches have been applied, such as (i) preparation of highly reactive ultrafine powders, (ii) introducing nonstoichiometry in Cr, and (iii) doping of cations at La and/or Cr sites. For reviews on the subject, see [1–5]. The co-doping of transition metals into Cr sites was also noted as beneficial in improving the sinterability and electrical conductivity [4–8]. The Pechini method [9], which offers high homogeneity, low temperature processing and high compositional flexibility via control of the processing variables, was also found better than the solid state reaction method for improving the air sinterability [7].

Pure LaCrO$_3$ is orthorhombic (space group: *Pnma*, 62; number of formula units in the unit cell, $Z = 4$) at room temperature and transforms to rhombohedral phase (space group: $R\bar{3}c$, 167; $Z = 6$) at ∼255 °C as observed using x-ray diffraction [10–12], neutron powder diffraction [12, 13], convergent-beam electron diffraction [14] and vibrational spectroscopy [15–18]. Doped LaCrO$_3$ arrests the structure: orthorhombic or rhombohedral or both, at room temperature, strongly depending on the dopant, its molar concentration and synthesis route [1, 6–8, 12, 19–24].

In the present paper, the effect of the composition on the structure of the novel perovskite system (La$_{1−x}$Sr$_x$)(Cr$_{0.85}$Fe$_{0.05}$Co$_{0.05}$Ni$_{0.05}$)O$_{3−\delta}$ (abbreviated as LSCFC′N) is investigated. The La site was doped with Sr^{2+} with composition $x = 0$–0.4 mole fraction and the Cr site was co-doped with 0.05 mol of Co^{2+}, Fe^{2+} and Ni^{2+}, using the Pechini method in order to increase the electrical conductivity and air sinterability without affecting the CTE of LaCrO$_3$ as well as to make it compatible with stainless steel, a metallic inter-connector/current collector for intermediate temperature solid oxide fuel cell (IT-SOFC) applications. The advantage of the system is that the composition of doped cations can be tailored to obtain a desired property. The aim of the present work is to explore the structure of the LSCFC′N with x using x-ray diffractometry (XRD), pycnometry, and Fourier-transform infrared (FT-IR) and Raman spectroscopy. The Scherrer formula was used for crystallite size calculation. The relative density was evaluated using theoretical and measured values of densities. Structural results were compared with those for orthorhombic LaCrO$_3$. A mechanism employing a partial-charge model was proposed to explain the results.

2. Experimental details

(La$_{1−x}$Sr$_x$)(Cr$_{0.85}$Fe$_{0.05}$Co$_{0.05}$Ni$_{0.05}$)O$_{3−\delta}$ (LSCFC′N) was prepared using the Pechini method. Commercially available starting precursors: La(NO$_3$)$_3$·xH$_2$O (99.9%, Aldrich), Sr(NO$_3$)$_2$ (99%, Aldrich), Cr(NO$_3$)$_3$·9H$_2$O (99%, Acros), (CH$_3$CO$_2$)$_2$Fe (95%, Acros), Co(NO$_3$)$_2$·6H$_2$O (99%, Aldrich) and Ni(NO$_3$)$_2$·6H$_2$O (99%, Acros) in molar weight proportion were dissolved in distilled water to get 0.3 M (40 ml) clear sol by stirring at room temperature for 2 h. The salts were dissolved as per their hydrolysis constants (pK$_{11}$) in the following order: Sr^{2+} (13.8), La^{3+} (10.7), Fe^{2+} (9.5), Co^{2+} (9.7), Ni^{2+} (9.4) and Cr^{3+} (4.4) in order to control hydrolysis– condensation reactions [25]. Ethylene glycol (C$_2$H$_6$O$_2$, 99%, Aldrich) of mass equal to the total mass of cations available was then added dropwise under stirring for improving the solubility and later esterification. Finally, chelating material, citric acid (C$_6$H$_8$O$_7$, 99.5%, Aldrich) of mass the same as the ethylene glycol, was added dropwise under stirring. The sol was stirred at ∼50 °C for 24 h and then left stirring at ∼70 °C to get homogeneous polymeric resin. The residual resin was then dried at ∼150 °C for 48 h, pre-calcined at ∼450 °C for 30 min, calcined at ∼900 °C for 2 h and finally sintered at ∼1100 °C for 2 h to get ultrafine perovskite powder.

A Rigaku x-ray diffractometer (D/Max 2500/K, Japan) with step 0.02°, scan speed $3°$ min^{-1} and range $20°$–$80°$ was used for phase identification of the powder sample. Structural analysis of the LSCFC′N was performed by the full-profile fitting method using a Rietveld analysis program: *MAUD* [26]. For the sample with $x = 0.1$, Rietveld refinement was performed for the orthorhombic perovskite phase and then the $SrCrO_4$ phase was introduced and refined again. For the samples with $x = 0.2$–0.4, the refinement was carried out for both the phases together. A program, Diamond [27], was used to calculate bond lengths and bond angles. The Scherrer formula: $D = 0.94\lambda/\beta\cos(\theta)$, where $\lambda = 1.540\,56$ Å and $\beta =$ full width at half-maxima, was used to calculate the average crystallite size (D) at $2\theta \sim 32.5°$ (main perovskite peak). The density (ρ_{m}) of the powder sample was measured using an Accupye 1330 Pycnometer (Micrometrics, USA). A Fourier-transform infrared spectrometer (Shimadzu, Prestige21, Japan, resolution 4 cm^{-1}), equipped with a KBr beam splitter, was used to record IR spectra of the sample (in the KBr pellet) in the range of 400–1000 cm^{-1}. A Jobin Yvon T64000 triple Raman spectrometer equipped with an Ar$^+$ ion laser source of wavelength 514.5 nm was employed for collecting the Raman spectra in the range 50–1000 cm^{-1} for 100 s (10 s $\times$ 10) in the backscattering geometry. The laser power at the polished surface of the dark pellet was kept at $\sim$2 mW using a 50$\times$ objective lens and spot area of $\sim$25 μm in order to minimize the overheating effect. The spectra were analysed quantitatively using *PSD* [28] and *OPUS* [29]. *PSD* offers Fourier self-deconvolution of complex spectra via interactive apodization and a deconvolution function, while *OPUS* combines curve fitting and deconvolution. The deconvolution function consists of Lorentz and Gauss functions. All experiments were performed in the open atmosphere at room temperature.

3. Results and discussion

3.1. X-ray diffractometry and pycnometry

Figure 1 shows x-ray diffractograms of the $(La_{1-x}Sr_x)(Cr_{0.85}Fe_{0.05}Co_{0.05}Ni_{0.05})O_{3-\delta}$ (LSCFC′N) for $x = 0$–0.4. Reflection peaks of orthorhombic $LaCrO_3$ perovskite (space group: *Pnma*, 62; $a = 5.476(1)$, $b = 7.752(2)$, $c = 5.512(1)$ Å; cell volume = 233.98 Å^3; theoretical density = 6.78 g cm^{-3}; JCPDS: 83-1327; [12]) have also been drawn for direct comparison. The orthorhombic phase was distinguished by a characteristic orthorhombic weak peak at $2\theta \sim 25.6°$ due to the (111) plane and the strongest peak at $2\theta \sim 32.5°$ due to the (121) plane with shoulders by (002) and (200) planes. A rhombohedral perovskite system exhibits a strong doublet of nearly equal intensities at $2\theta \sim 32.3°$–$32.8°$ [19]. Monoclinic $SrCrO_4$ ($P2_1/c$ space group, 14; $a = 7.0897(4)$, $b = 7.3939(4)$, $c = 6.7553(6)$ Å; cell volume = 344.76 Å^3; density = 3.92 g cm^{-3}; JCPDS 35-0743), marked by asterisks in the XRD pattern, was noticed as a second phase for the samples with $x \geqslant 0.1$, which is common in the Sr^{2+} doped $LaCrO_3$ samples prepared by sol–gel method and/or sintered below 1400 °C [7, 20, 23]. This is most probably due to a large difference in the hydrolysis rates of Sr^{2+} and Cr^{3+} ions, where anions also play a key role [25].

The XRD data were then refined using *MAUD* in order to collect crystallographic parameters of the LSCFC′N with increasing x. For $x \geqslant 0.1$, Rietveld refinement was performed for the biphasic system of orthorhombic perovskite and $SrCrO_4$ with the help of the crystallographic parameters of orthorhombic $LaCrO_3$ of *Pnma* space group (table 1) [12] and monoclinic $SrCrO_4$ of $P2_1/c$ space group (table 2) [30], respectively. Subsequently, weight fractions of the phases were obtained. The site occupancies were kept at fixed values consistent with the nominal stoichiometry. It is also worth pointing out that the B factor for the Cr atom of $LaCrO_3$ is negative. According to Khattak and Cox [12], it is probably an experimental

3
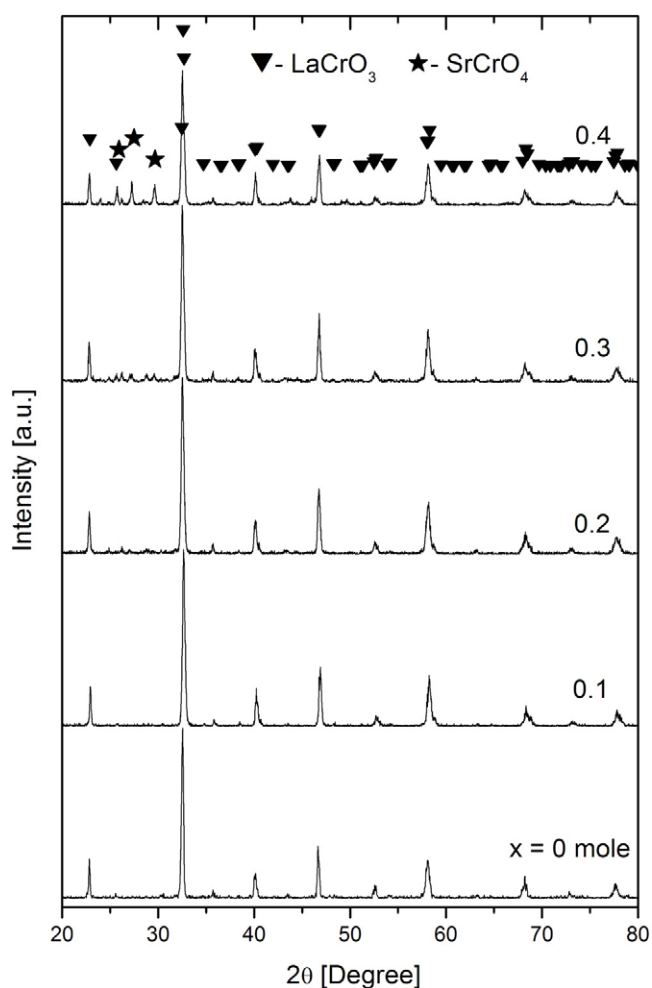
Figure 1. X-ray diffractograms of $(La_{1-x}Sr_x)(Cr_{0.85}Fe_{0.05}Co_{0.05}Ni_{0.05})O_{3-\delta}$ for $x = 0$–0.4.

artefact resulting from the low value of the scattering amplitude for Cr and the data only extend to a $\sin\theta/\lambda$ value of 0.34. They also mentioned that it could arise from deficiencies in the model such as the neglect of anisotropic terms. However, the negative B factor of Cr does not affect the refinement significantly and hence the structural results, as observed earlier for the orthorhombic $LaCrO_3$ [13] and $La_{0.75}Sr_{0.25}CrO_3$ [24] including the LSCFC′N. Figures 2(a) and (b) show final Rietveld plots for the LSCFC′N with $x = 0$ exhibiting a single perovskite phase and the $x = 0.4$ sample containing mixed phases, respectively. The observed and calculated intensity profiles were well matched, which is obvious from their difference as shown at the bottom of the figures 2(a) and (b). The composition dependent crystallographic parameters and the refinement parameters (S and R) for the LSCFC′N are listed in table 1. The R values were found close to each other for all values of x. The values of the goodness of fit (S) were also found close to each other for $x = 0.1$–0.4. These indicate good quality of the profile fittings. However, the value of S for $x = 0$ is found higher than those for $x = 0.1$–0.4 probably due to an unknown phase exhibiting a small peak at $2\theta \sim 35.7°$ and marked by an arrow in the figure 2(a). Table 3 shows the values of the lattice parameters for the $SrCrO_4$ phase
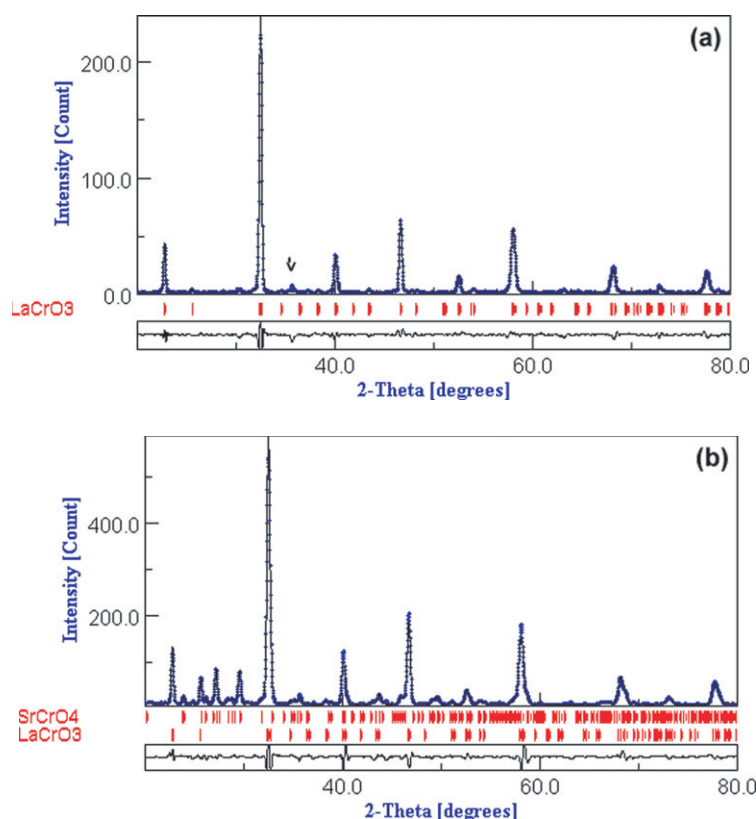
Figure 2. Rietveld refined profiles of the $(La_{1-x}Sr_x)(Cr_{0.85}Fe_{0.05}Co_{0.05}Ni_{0.05})O_{3-\delta}$ with $x = 0$ (a) and 0.4 (b). The solid line is calculated intensity and the plus is observed intensity (the background was not subtracted). The short vertical lines show the possible Bragg reflections. The bottom corresponds to the difference between observed and calculated intensities. An arrow in (a) corresponds to an unknown phase.

determined from the samples with $x = 0.1$–0.4, which became closer to the reported values of the pure $SrCrO_4$ for $x = 0.3$ and 0.4 probably due to high amount of the impurity phase. Figure 3 shows lattice constants (a, b and c) and cell volume (V) of the LSCFC'N with x. One can note an increase in the volume of LSCFC'N ($x = 0$) with respect to $LaCrO_3$. However, substitution of La^{3+} by Sr^{2+} ($x = 0.1$–0.4) sharply decreased the volume of LSCFC'N by decreasing the lattice constants, though the ionic radius of Sr^{2+} (1.44 Å) was larger than that of La^{3+} (1.36Å). For $x \geqslant 0.1$, the volume was almost invariant. These results are similar to those observed earlier for several doped and co-doped $LaCrO_3$ systems [5–8, 21, 22] as well as $La_{1-x}Sr_xCo_{0.2}Fe_{0.8}O_3$ (LSCF), $La_{1-x}Sr_xCo_{0.9}Ni_{0.1}O_3$ (LSCN) and $La_{1-x}Sr_xFe_{0.9}Ni_{0.1}O_3$ (LSFN) [31, 32], and can be explained in terms of the ionic radius and mixed valence states of transition metal ions, which has been discussed below.

Substitution of a lower valence ion at La and/ or Cr sites of $LaCrO_3$ results in a charge-compensating transition of Cr^{3+} to Cr^{4+} ions [1]. The greater charge density of the Cr^{4+} favours the contraction of the Cr−O bonds and decrease of the unit cell volume. Mori *et al* [7] found that doping of Co and/or Al ions into Cr sites of the $La_{0.9}Sr_{0.1}CrO_3$ transforms trivalent cations into tetravalent cations of small ionic radii. Doping of Co and/or Ni ions into Cr sites of $La_{0.85}Sr_{0.15}CrO_3$ also transforms some of the Cr^{3+} ions into Cr^{4+} of smaller ionic radius [8].
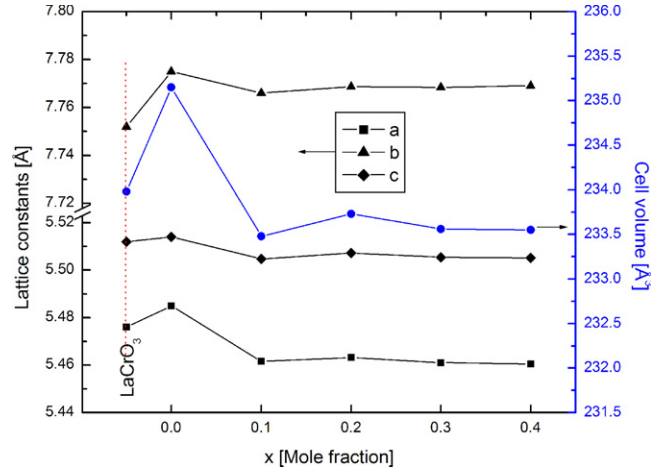
Figure 3. Lattice constants (a, b and c) and cell volume pure orthorhombic LaCrO$_3$ and $(La_{1-x}Sr_x)(Cr_{0.85}Fe_{0.05}Co_{0.05}Ni_{0.05})O_{3-\delta}$ ($x = 0$–0.4). The line guides the eye.

Table 1. Wyckoff notation, lattice constants (a, b and c), fractional atomic coordinates (x, y and z), atomic displacement factor (B_{iso}) and refinement parameters (goodness of fit, S and R factor) for the orthorhombic perovskite systems of *Pnma* space group: LaCrO$_3$ [12] and $(La_{1-x}Sr_x)(Cr_{0.85}Fe_{0.05}Co_{0.05}Ni_{0.05})O_{3-\delta}$ ($x = 0$–0.4). Numbers in parentheses are statistical errors of the last significant digit. (Note: Wyckoff notation of atoms. La/Sr: 4c (x, 0.25, z), Cr/(Fe–Co–Ni): 4b (0, 0, 0.5), O1: 4c (x, 0.25, z) and O2: 8d (x, y, z).)

| Atom | Parameters | LaCrO$_3$ | $(La_{1-x}Sr_x)(Cr_{0.85}Fe_{0.05}Co_{0.05}Ni_{0.05})O_{3-\delta}$ | | | | |
			$x = 0$	$x = 0.1$	$x = 0.2$	$x = 0.3$	$x = 0.4$
	a (Å)	5.476(1)	5.485(1)	5.4616(7)	5.4632(5)	5.4610(6)	5.4605(6)
	b (Å)	7.752(2)	7.775(1)	7.767(1)	7.7686(9)	7.7684(1)	7.7695(1)
	c (Å)	5.512(1)	5.514(1)	5.5045(6)	5.5072(5)	5.5055(7)	5.5052(6)
La	x	0.0196(4)	0.0172(6)	0.0130(5)	0.0090(7)	0.0143(6)	0.006(1)
	z	−0.0046(5)	0.0174(5)	0.003(3)	0.000(2)	−0.001(2)	−0.000(2)
	B_{iso} (Å^2)	0.1(1)	3.3(1)	3.94(7)	0.10(5)	0.22(6)	0.04(3)
Cr	B_{iso} (Å^2)	−0.4(1)	2.8(1)	2.9(1)	2.7(1)	0.4(1)	0.7(1)
O1	x	0.4935(6)	0.438(1)	0.496(2)	0.484(4)	0.454(3)	0.494(7)
	z	0.0676(4)	0.214(1)	0.02(1)	0.013(1)	0.074(6)	0.036(6)
	B_{iso} (Å^2)	0.1(1)	3.0(2)	0.2(1)	0.32(8)	0.41(8)	0.5(2)
O2	x	0.2265	0.203(5)	0.25(1)	0.219(4)	0.189(3)	0.211(6)
	y	0.5338	0.497(4)	0.550(5)	0.444(2)	0.533(5)	0.551(5)
	z	0.2265(3)	0.269(7)	0.26(1)	0.261(6)	0.262(4)	0.25(1)
	B_{iso} (Å^2)	0.3(1)	1.9(5)	2.4(2)	2.1(3)	0.2(1)	0.6(9)
	S (%)	—	45.6	36.0	25.2	23.2	22.8
	R (%)	—	15.9	12.6	11.7	12.5	12.6

Liu *et al* [21] showed through XPS study that introduction of Sr^{2+} in the La sites enhances the transformation of Cr^{3+} to Cr^{6+} of smaller ionic radius. Tai *et al* [31] successfully proposed for the LSCF that the trivalent cations (M^{3+}, M $=$ Co or Fe) transform to the high and low valence cations as $2M^{3+} \Leftrightarrow M^{2+} + M^{4+}$, which is a reversible process. Similarly, two M^{4+} ions can form M^{3+} ions. It was also shown that the concentration of M^{2+}, M^{3+} and M^{4+} depends on the

Table 2. Wyckoff notation, fractional atomic coordinates (x, y and z) and atomic displacement factor (B_{iso}) for SrCrO$_4$ (monoclinic; space group: $P2_1/c$, 14) [30].

Atom	Wyckoff notation	x	y	z	B_{iso} (Å^2)
Sr	4e	0.1024	0.3561	0.7694	3.0(5)
Cr	4e	0.5973	0.3156	0.8060	2.9(5)
O1	4e	0.7264	0.3521	0.6001	5.9(5)
O2	4e	0.4577	0.5287	0.7504	5.9(5)
O3	4e	0.7868	0.3884	0.9585	5.9(5)
O4	4e	0.5023	0.1826	0.8435	5.9(5)

Table 3. Lattice constants (a, b, c and β) and unit cell volume (V) of monoclinic SrCrO$_4$ phase observed in the samples of $(La_{1-x}Sr_x)(Cr_{0.85}Fe_{0.05}Co_{0.05}Ni_{0.05})O_{3-\delta}$ with $x = 0.1$–0.4. Reported values of lattice parameters for the pure SrCrO$_4$ are also shown. Numbers in parentheses are statistical errors of the last significant digit.

x	a (Å)	b (Å)	c (Å)	Angle (deg)	V (Å^3)	Reference
Pure	7.0897(4)	7.3939(4)	6.7553(6)	103.197(5)	344.76	JCPDS 35-0743
Pure	7.07(3)	7.33(6)	6.73(3)	103.9(6)	338.56	[30]
0.1	6.990(2)	7.529(2)	6.700(2)	104.30(2)	341.68	This work
0.2	6.991(2)	7.539(2)	6.707(2)	104.33(2)	342.49	This work
0.3	7.044(2)	7.468(2)	6.760(2)	104.41(5)	344.42	This work
0.4	7.098(1)	7.401(1)	6.770(1)	103.27(1)	346.15	This work

Sr^{2+} concentration and ambient temperature. According to Huang *et al* [32], a charge transfer takes place for the LSCN and LSFN in the following way: $M^{3+} + Ni^{3+} \Leftrightarrow Ni^{2+} + M^{4+}$. This mechanism can also be utilized to explain the compositional variation of the cell volume for the LSCFC′N. Thus, an increase in volume with respect to pure LaCrO$_3$ is most probably due to larger ionic radii of doped cations: Fe^{2+} (0.78 Å), Co^{2+} (0.74 Å) and Ni^{2+} (0.69 Å) compared to that of Cr ions (3+, 0.61 Å; 4+, 0.55 Å), while the invariance in the volume for $x \geqslant 0.1$ can be attributed to the transformation of some of transition metal ions into their higher valence states of smaller ionic radii (Cr^{6+}, 0.44 Å; Fe^{3+}, 0.64 Å; Co^{3+}, 0.54 Å; Ni^{3+}, 0.56 Å). This study is further supported by the bond length determination, discussed below.

Figure 4 shows the measured (ρ_m), theoretical (ρ_{th}) and relative ($\rho = \rho_m/\rho_{th}$) densities versus x plots for the LSCFC′N. These variations are found similar to those observed for the LSCF with increasing x [31]. The theoretical density was found decreased almost linearly with increasing x due to a linear decrease in the formula weight of the LSCFC′N. For the $x \geqslant 0.2$, ρ_m and hence ρ deviated greatly from the trend of ρ_{th}. Since the weight faction (γ) of the low density SrCrO$_4$ is relatively high for $x \geqslant 0.2$, as evidenced in the inset of figure 4 showing a linear increase of the second phase with increasing x, one may guess it to be one of the causes for the large deviation. This can be verified tentatively by considering the total theoretical density (ρ_T) of the sample as $\rho_T = (1 - \gamma)\rho_{th} + \gamma\rho_l$ and determining the pseudo-relative density (ρ') using the relation $\rho' = \rho_m/\rho_T$, where ρ_l (=3.92 g cm^{-3}) is the theoretical density of the SrCrO$_4$. The values of ρ' for $x = 0.2$–0.4 were varied from 0.92 to 0.94 and comparable to that for $x = 0$ and 0.1 ($\sim$0.91), which is in agreement with the above mentioned conjecture.

Any volumetric change in LaCrO$_3$ perovskite is due to the deformation of LaO$_{12}$ and CrO$_6$ polyhedra by changing bond lengths (La−O and Cr−O) and bond angle (Cr−O−Cr) [13, 16, 17, 24]. The average bond lengths, ⟨La−O⟩ and ⟨Cr−O⟩, of the LSCFC′N, evaluated using Diamond for $x = 0$–0.4, are plotted in figure 5. Average bond lengths of pure orthorhombic LaCrO$_3$ are also included in figure 5 for direct
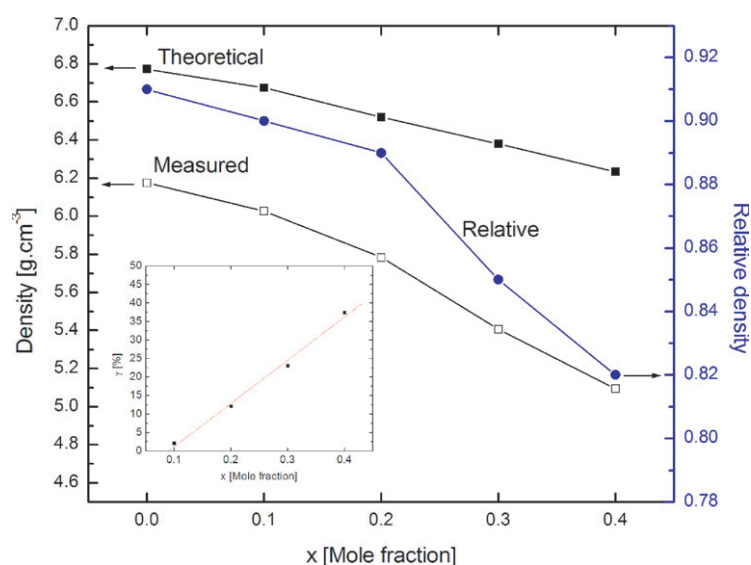
Figure 4. Various densities of $(La_{1-x}Sr_x)(Cr_{0.85}Fe_{0.05}Co_{0.05}Ni_{0.05})O_{3-\delta}$ ($x = 0$–0.4). Inset: a linear weight fraction (γ) of $SrCrO_4$ versus x plot. The line guides the eye.

comparison [12, 13]. For the LSCFC′N with $x = 0$, co-doping of a small fraction of Fe^{2+}, Co^{2+} and Ni^{2+} into Cr sites greatly increased ⟨Cr−O⟩ and slightly decreased ⟨La−O⟩ as expected, leading to an increased volume with respect to pure $LaCrO_3$. For $x = 0.1$, ⟨Cr−O⟩ was greatly decreased and ⟨La−O⟩ was slightly increased with respect to the values for $x = 0$, indicating a decrease in the volume. Further increase in x led to bond lengths and, hence, volume being almost invariant. These observations are further supported by variation of the average crystallite size (D) with x, which is shown in figure 6. The crystallite size was greatly decreased for $x = 0.1$ and then decreased insignificantly for higher values of x, as expected due to a large decrease in the Cr−O bond length for $x = 0.1$ and then almost invariance of the bond lengths for the higher x. The average bond angle (⟨Cr−O−Cr⟩), determined by Diamond, was used to calculate the tilt angle (ω) with the help of expression $\omega = (180° − ⟨Cr−O−Cr⟩)/2$. The tilt angle ($\omega$) represents the distortion of the CrO_6 with respect to the cubic phase ($\omega = 0°$) and its compositional variation was found identical to the V–x plot [24, 33]. Figure 5 shows the tilt angle versus x variation of the LSCFC′N, which is also almost identical to the V–x plot (figure 3), indicating a decrease in the orthorhombic distortion for $x = 0.1$, which remained almost invariant for higher x. These observations are further supported by spectroscopy studies, which have been discussed in section 3.2.

The compositional variation of the structural parameters and formation of the impurity phase can be explained using the partial-charge model [25, 34, 35]. According to this model, water present in the solution solvates the metal cation (M^{z+}, where z is charge) and anion ($X^- = NO_3^-$). This results in the formation of strong acid, HNO_3 ($pK_a = -1.3$) in the sol along with hydrolysis of cations in the form of aqua $[M(OH_2)_N]^{z+}$, hydroxo $[M(OH)_N]^{(N-z)+}$ or aqua-hydroxo $[M(OH)_h(OH_2)_{N-h}]^{(z-h)+}$, where $N (=6)$ is the coordination number of water molecules covalently bound to the cation and h is the molar ratio of hydrolysis. The anion complexes with the solvated metal cation if $\delta(X) > -1$ or $\chi(X^-) < \chi[M(OH_2)_{N-1}]^{z+} < \chi(H_2O)$, where δ and χ correspond to the electronegativity and the partial charge, respectively for the fully coordinated cations and pH is less than 7. Since $\chi(NO_3^-) = 2.76 > \chi(H_2O) = $
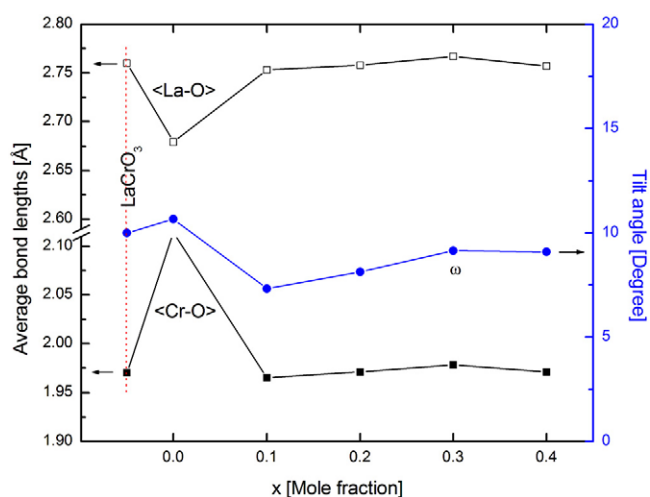
Figure 5. Average bond lengths ($\langle$La$-$O$\rangle$ and $\langle$Cr$-$O$\rangle$) and tilt angle (ω) of pure orthorhombic LaCrO$_3$ and (La$_{1-x}$Sr$_x$)(Cr$_{0.85}$Fe$_{0.05}$Co$_{0.05}$Ni$_{0.05}$)O$_{3-\delta}$ ($x = 0$–0.4). The line guides the eye.
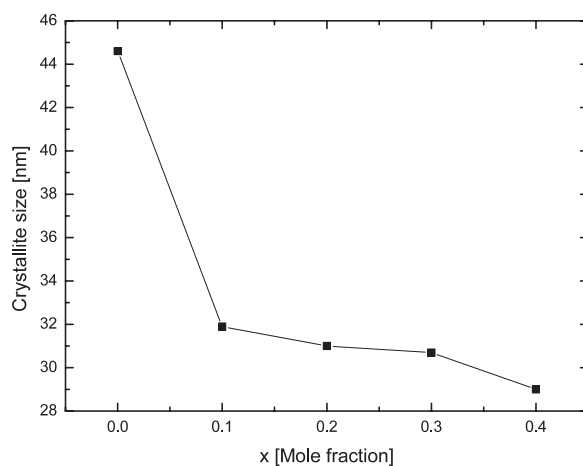
Figure 6. Crystallite size of (La$_{1-x}$Sr$_x$)(Cr$_{0.85}$Fe$_{0.05}$Co$_{0.05}$Ni$_{0.05}$)O$_{3-\delta}$ with $x = 0$–0.4. The line guides the eye.

2.49, one can expect electron transfer from the sol to the NO$_3^-$. This increases the charge negativity of the NO$_3^-$ giving rise to more ionic M^{z+}–NO$_3^-$ bonds. As Sr^{2+} is less acidic than La^{3+} [25], one can expect a slight decrease in acidity or a slight increase in the pH of the sol with increasing x, and hence a decrease in ionic bonding. An application of low temperature heat treatment promotes the metal citrate complex formation by chelating the metal ions in solution with pH dependent citric acid [36–38]. Hence, a better complexation is achieved with increasing x. The hydroxyl groups of ethylene glycol get attached with terminal carboxyl groups of metal citrate resulting in a homogeneous three-dimensional network of La^{3+} polymer–Sr^{2+} polymer–Cr^{3+} polymer–Fe^{2+} polymer–Co^{2+} polymer–Ni^{2+} polymer along with a small amount of impurity network, Sr^{2+} polymer–Cr^{3+} polymer. The impurity network gets formed probably due to the large ionic radius and high polarizability of the Sr^{2+}, where the
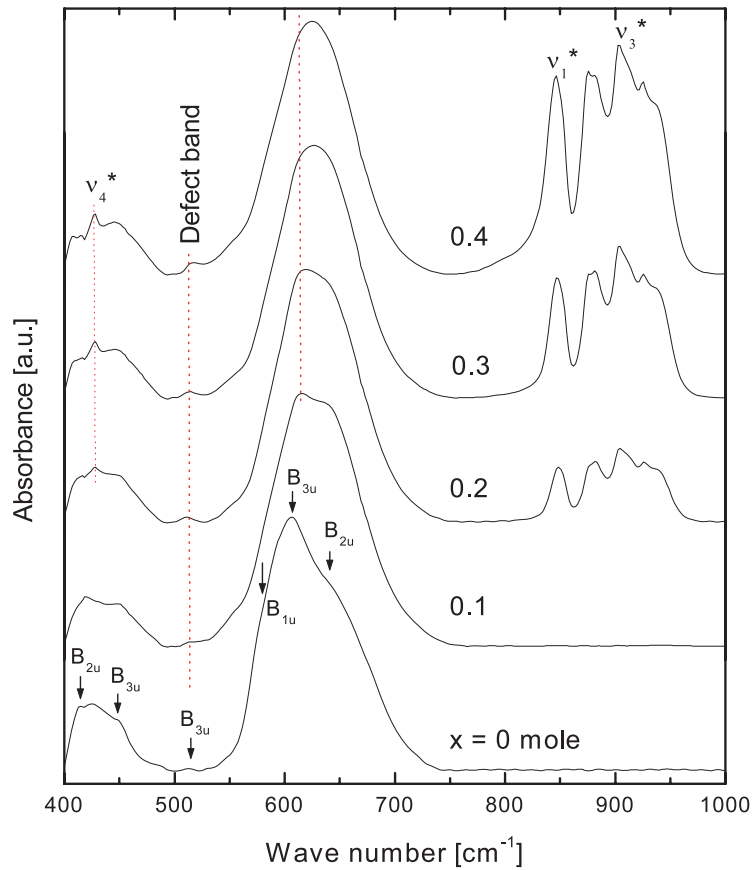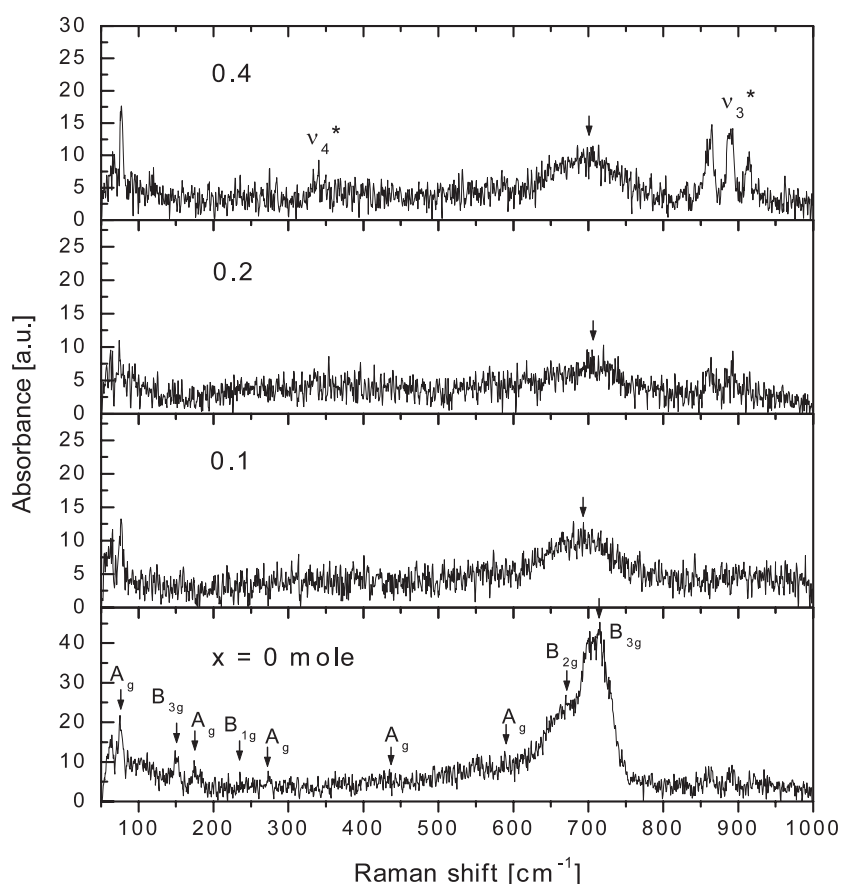
Figure 7. FT-IR spectra of $(La_{1-x}Sr_x)(Cr_{0.85}Fe_{0.05}Co_{0.05}Ni_{0.05})O_{3-\delta}$ with $x = 0$–0.4. Asterisk: $SrCrO_4$ phase.

hydrolysis rates of Sr^{2+} and Cr^{3+} also play a vital role [25, 38]. The homogeneity of polymer resin increases with increasing x, which in turn improves the morphology of the particles after pyrolysis as reported [39] and also observed in the D versus x variation (figure 6), which is identical to the V–x variation. An increase in the Sr^{2+} content also promotes forming more impurity network, which increases the second phase amount.

3.2. FT-IR and Raman spectroscopy

Figures 7 and 8 show IR and Raman spectra, respectively, of the $(La_{1-x}Sr_x)(Cr_{0.85}Fe_{0.05}Co_{0.05}Ni_{0.05})O_{3-\delta}$ (LSCFC′N) with $x = 0$–0.4. Owing to the resemblance with FT-IR and Raman spectra of pure orthorhombic $LaCrO_3$ [15–18] and $LaMnO_3$ [15, 16, 33, 40–43], and the well established fact that the atomic vibrations are almost the same for RMO_3 (R: rare earth element; M: transition metal) [15, 16, 33, 40, 42], the irreducible representation of the optical modes is presented as $\Gamma_{opt} = \Gamma_{Raman} + \Gamma_{IR} + \Gamma_{inactive} + \Gamma_{acoustic}$, with Raman active modes (24), $\Gamma_{Raman} = 7A_g + 5B_{1g} + 7B_{2g} + 5B_{3g}$; IR active modes (25), $\Gamma_{IR} = 9B_{1u} + 7B_{2u} + 9B_{3u}$; inactive modes (8), $\Gamma_{Inactive} = 8A_u$ and acoustic modes (3), $\Gamma_{Acoustic} = B_{1u} + B_{2u} + B_{3u}$. Similarly, the site symmetry of an orthorhombic $LaCrO_3$ based system can be represented as $La(C_s)$, $Sr(C_i)$, $O1(C_s)$ and $O2(C_1)$. Modes are also assigned on the basis

Figure 8. Raman spectra of $(La_{1-x}Sr_x)(Cr_{0.85}Fe_{0.05}Co_{0.05}Ni_{0.05})O_{3-\delta}$ for $x = 0, 0.1, 0.2$ and 0.4. Asterisk: $SrCrO_4$ phase.

of lattice dynamical calculations (LDC) [33, 40, 41] and observed values for orthorhombic $LaMnO_3$ [15, 16, 33, 40, 41], which are shown in table 4 as well as in figures 7 and 8. The high frequency Cr–O stretching vibration region consists of IR active modes: B_{2u} (apical), B_{3u} (in-plane) and B_{1u} (in-plane oxygen vibration), and Raman active modes: B_{3g} (out of phase, breathing), B_{2g} (in phase) and A_g (in phase). In the mid-frequency region, bending and titling modes exist due to deformation of octahedral CrO_6. The IR active bending modes are B_{3u} (in plane), B_{1u} (apical), B_{3u} (apical) and B_{2u} (in-plane oxygen vibration). Similarly, Raman active A_g mode corresponds to CrO_6 octahedral out-of-phase bending. Raman active tilt modes, A_g and B_{1g}, correspond to in-phase and out-of-phase CrO_6 y rotational distortions, respectively. Low frequency Raman active lattice modes, namely, A_g, B_{3g} and A_g involving mixed vibrations of La and O1 atoms along z, y and x axes, respectively, exist due to relative motion of CrO_6 against the surrounding La/Sr cage.

It is obvious from the figures that the bands are broad most probably due to loss of degeneracy upon lowering of the symmetry of the octahedron and the increase of the unit cell to more than one ABO_3 unit [15, 16]. The doping-induced disorder due to the changed mass, charge, and lattice parameters broadens the bands too. However, reduction in orthorhombic distortion reduced the intensity and/or number of bands [42, 43]. One can also note that almost

Table 4. Observed vibrational bands in (cm^{-1}) and possible assignments for $(La_{1-x}Sr_x)(Cr_{0.85}Fe_{0.05}Co_{0.05}Ni_{0.05})O_{3-\delta}$ with respect to $LaCrO_3$ [15–18] and $LaMnO_3$ (Raman [33, 40], IR [41]). Superscripts a–d correspond to [15–18], respectively. Note: notation: s, strong; m, medium; w, weak; sp, sharp; sh, shoulder; b, broad relative intensity.

| | $LaMnO_3$ | | $LaCrO_3$ | $(La_{1-x}Sr_x)$ $(Cr_{0.85}Co_{0.05}Fe_{0.05}Ni_{0.05})O_{3-\delta}$ | |
Mode	Exp.	LDC	Exp.	$x = 0$	$x = 0.1$–0.4
			IR (400–1000 cm^{-1})		
B_{2u}/apical oxy. vib.—stretching	621 sh	625	640[a] s,b	640 sh	644–641 sh
B_{3u}/in-plane oxy. vib.—stretching	594 s, b	580	630[a], 606[c] s	606 s, b	612–615 s, b
B_{1u}/in-plane oxy. vib.—stretching	574 sh	577	580[a] s,b, 585[b], 573[c] sh	582 sh	585–586 sh
B_{3u}/in-plane oxy. vib.—bending	510 m, b	521	493[c] sh	513 w, b	514–517 m, b
B_{1u}/apical oxy. vib.—bending	469 sh	495	471[c] sh	—	—
B_{3u}/apical oxy. vib.—bending	455 sh	443	446[c] sh	449 sh	449–445 sh
B_{2u}/in-plane oxy. vib.—bending	416 s, b	412	425[a] s,b, 407[b] sp, 425[c] s	413 sp, b	419–415 b
			Raman (50–1000 cm^{-1})		
B_{3g}/out-of-phase stretching	—	692	719[c] s	716 s	716–715 sh
B_{2g}/in-phase stretching	611	669	675[c], 695[d] sh	671 sh	694–700 s, b
A_g/in-phase stretching	—	582	590[c], 581[d] s	590 m	575–586 w
A_g/out-of-phase bending	493	480	441[c], 427[d] s	436 m	471–476 w
A_g/in-phase y rotations—tilt	257	246	279[c] w	274 m	268–271 w
B_{1g}/out-of-phase y rotations—tilt	—	254	252[c], 253[d] b,s	237 w	258–256 w
A_g/Lattice vibration (z)	198	162	174[c], 172[d] s	175 s	—
B_{3g}/Lattice vibration (y)	—	158	150[c], 149[d] s	150 s	157–160 s
A_g/Lattice vibration (x)	140	81	71[c] sh (−196 °C)	77 s	78–79 s

all $LaCrO_3$ bands appeared distinctively in the spectra of the LSCFC′N with $x = 0$. The spectra of the LSCFC′N for $x = 0.1$–0.4 were also found almost identical in nature resulting in the band positions being almost invariant. It is also worth mentioning that the bending modes of pure perovskite phase and the second phase fall into the same domain of wavenumber. Some noteworthy features observed with increasing x are as follows; they have been explained on the basis of reported observations [33, 40–43].

(i) In the high frequency stretching vibration region, B_{3u} (in-plane, IR) and B_{3g} (out-of-phase, Raman) modes were prominent, while B_{2u} (apical, IR) and B_{2g} (out-of-phase, Raman) modes were at the shoulders. However, substitution of La^{3+} by Sr^{2+} ($x = 0.1$–0.4) made these modes almost equal in intensity with greatly upshifted B_{3u} (IR) and B_{2g} (Raman) modes. This corresponds to a decrease of Cr−O bond length. Initially, the band positions of B_{3u} and B_{2g} for the LSCFC′N ($x = 0$) were lower than those for pure $LaCrO_3$ indicating a large Cr−O bond length for sample with $x = 0$.

(ii) The bending modes, B_{2u} (in plane, IR) and A_g (out of phase, Raman) were decreased initially for $x = 0$ with respect to pure $LaCrO_3$, then increased for higher values of x, indicating an initial decrease and then an increase in the La−O bond length as the shift in bending mode is proportional to the La−O bond length.

(iii) The tilting mode, A_g (in phase, Raman) at ∼274 cm^{-1} for $x = 0$ was decreased to 268 cm^{-1} for $x = 0.1$, which remained almost constant for higher x. Since the tilt mode is proportional to the tilt angle (ω) and inversely proportional to the ionic radius of the La site, one can expect a decrease in ω and an increase in ionic radius of the La site.
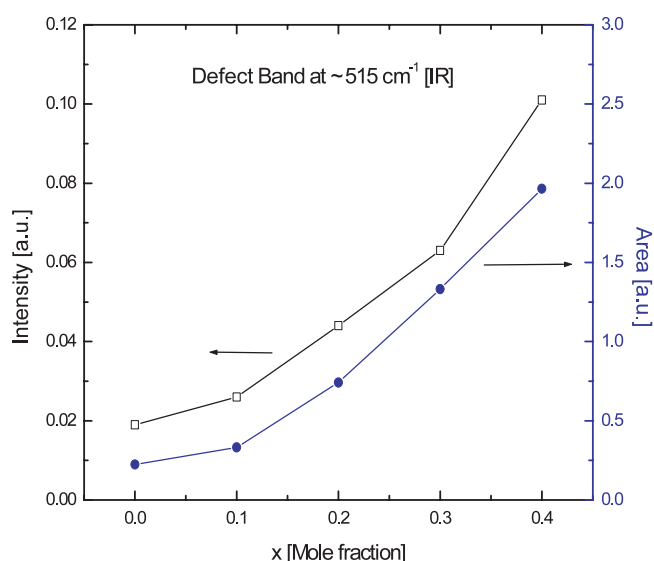
Figure 9. IR intensity and area of the defect band for $(La_{1-x}Sr_x)(Cr_{0.85}Fe_{0.05}Co_{0.05}Ni_{0.05})O_{3-\delta}$ with $x = 0$–0.4. The line guides the eye.

(iv) The charge replacement of La^{3+} via doping with Sr^{2+} strengthened the force constant between CrO_6 and La as observed from the higher value of the lattice mode, $B_{3g}(y)$, for $x = 0.1$–0.4 with respect to the undoped system ($x = 0$).

(v) The mid-frequency IR active bending mode B_{3u} (in plane) at ~ 515 cm^{-1} was assigned as a defect band by Kuznetsova *et al* [44] due to distortion in the CrO_6 octahedra by the high valence cations. The IR intensity and area of defect band were increased with increasing x, as shown in figure 9. This was also confirmed by the existence of additional peaks in the high frequency region (>750 cm^{-1}) of Raman spectra [17]. This results in structural rearrangement and stacking disordering in the perovskite phase [17, 44]. This supports well our finding that the structural parameters are almost invariant for $x \geqslant 0.1$ due to an increase in the number of high valence cations.

The presence of the second phase, $SrCrO_4$ (site symmetry, C_1), was confirmed from the following $SrCrO_4$ characteristic bands. Cr−O stretching mode, ν_3, IR: ~ 925 (925), ~ 912 (912), 883 (890); Raman: ~ 927 (929), ~ 914 (915), ~ 864 (866 cm^{-1}). Cr−O stretching mode, ν_1, IR: ~ 847 (843). O−Cr−O bending mode, ν_4, IR: ~ 428 (434), ~ 408 (408); Raman: ~ 395 (~ 395 cm^{-1}). O−Cr−O bending mode, ν_2, IR: (344); Raman: ~ 340 (~ 340 cm^{-1}). The data in parentheses refer to the reported IR [45] and Raman [46] bands of $SrCrO_4$. Figure 10 shows IR and Raman intensities of $SrCrO_4$ bands: ν_1 (IR) and ν_3 (Raman) with increasing x. The intensities of the bands increased linearly with increasing x, indicating a linear increase in the amount of the second phase, which is in good agreement with the XRD study (figure 4).

4. Conclusions

A new perovskite system, $(La_{1-x}Sr_x)(Cr_{0.85}Fe_{0.05}Co_{0.05}Ni_{0.05})O_{3-\delta}$, was prepared via doping at the La site with Sr^{2+} to a concentration $x = 0$–0.4 mole fraction and at the Cr site with 0.05 mol of Fe^{2+}, Co^{2+} and Ni^{2+}, using the Pechini method. The advantage of the system is that the composition of doped cations can be tailored to obtain a desired property. X-
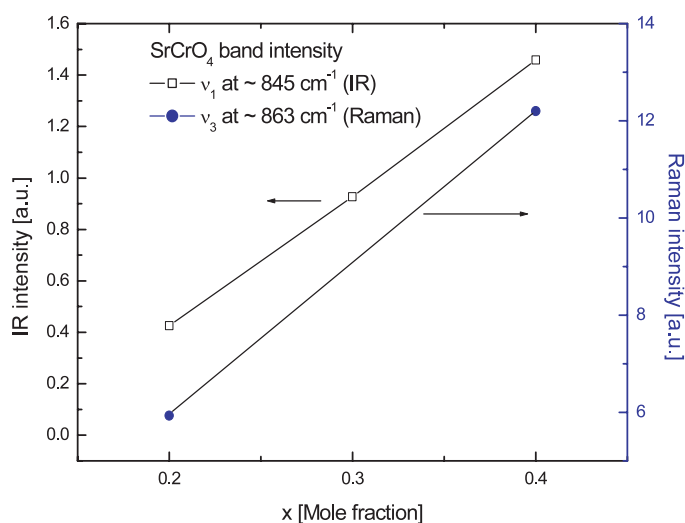
Figure 10. IR and Raman intensity of the stretching bands due to $SrCrO_4$ observed in $(La_{1-x}Sr_x)(Cr_{0.85}Fe_{0.05}Co_{0.05}Ni_{0.05})O_{3-\delta}$ with $x = 0.2$–0.4. The line guides the eye.

ray diffractometry, pycnometry, and Fourier-transform infrared and Raman spectroscopy were employed for structural study and the results were compared with those for orthorhombic $LaCrO_3$. Samples exhibited orthorhombic perovskite structure with *Pnma* space group along with a second phase, monoclinic $SrCrO_4$, which increased in content with increasing x. A large lattice and hence volume contraction was noticed for $x = 0.1$, which was accompanied by a sharp decrease in the bond lengths, tilt angle and crystallite size due to the transformation of some transition metal ions into their higher valence states of smaller ionic radii, as supported by the presence of a defect band (~ 515 cm^{-1}, IR). For $x = 0.1$–0.4, the structural parameters were almost invariant. The structural results were corroborative with the shift of the octahedral CrO_6 stretching, bending and tilting bands. A mechanism employing a partial-charge model was proposed to explain the results.

Acknowledgments

References

[1] Minh N Q 1993 *J. Am. Ceram. Soc.* **76** 563
[2] Steele B C H and Heinzel A 2001 *Nature* **414** 345
[3] Sfeir J 2003 *J. Power Sources* **118** 276
[4] Zhu W Z and Deevi S C 2003 *Mater. Sci. Eng.* A **348** 227
[5] Fergus J W 2004 *Solid State Ion.* **171** 1
[6] Gordes P and Christiansen N 1993 *Proc. Electrochem. Soc.* **93–94** 414
[7] Mori M and Sammes N M 2002 *Solid State Ion.* **146** 301
[8] Ding X, Liu Y, Gao L and Guo L 2006 *J. Alloys Compounds* **425** 318

 [9] Pechini M 1967 *US Patent* 3330697
[10] Geller S 1957 *Acta Crystallogr.* **10** 243
[11] Geller S and Raccah P M 1970 *Phys. Rev.* B **2** 1167
[12] Khattak C P and Cox D E 1977 *Mater. Res. Bull.* **12** 463
[13] Oikawa K, Kamiyama T, Hashimoto T, Shimojyo Y and Morii Y 2000 *J. Solid State Chem.* **154** 524
[14] Hashimoto T, Takagi K, Tsuda K, Tanaka M, Yoshida K, Tagawa H and Dokiya M 2000 *J. Electrochem. Soc.* **147** 4408
[15] Rao G V S, Rao C N R and Ferraro J R 1970 *Appl. Spectrosc.* **24** 436
[16] Daturi M, Busca G and Willey R J 1995 *Chem. Mater.* **7** 2115
[17] Tompsett G A and Sammes N M 2004 *J. Power Sources* **130** 1
[18] Orlovskaya N, Coratolo A, Johnson C and Gemmen R 2004 *J. Am. Ceram. Soc.* **87** 1981
[19] Khattak C P and Cox D E 1977 *J. Appl. Crystallogr.* **10** 405
[20] Simner S, Hardy J, Stevenson J and Armstrong T 1999 *J. Mater. Sci.* **34** 5721
[21] Liu X, Su W, Lu Z, Liu J, Pei L, Liu W and He L 2000 *J. Alloys Compounds* **305** 21
[22] Berger D, Jitaru I, Stanica N, Perego R and Schoonman J 2001 *J. Mater. Synth. Process.* **9** 137
[23] Duran P, Tartaj J, Capel F and Moure C 2004 *J. Eur. Ceram. Soc.* **24** 2619
[24] Chakraborty K R, Yusuf S M, Krishna P S R, Ramanadham M, Tyagi A K and Pomjakushin V 2006 *J. Phys.: Condens. Matter* **18** 8661
[25] Pierre A C 1998 *Introduction to Sol–Gel Processing* (Boston, MA: Kluwer–Academic) pp 30–77
[26] Lutterotti L 2006 *MAUD* Version 2.044 Itali
[27] Brandenburg K 2006 *Diamond* Version 3.1d Germany
[28] Kochev N T, Rogojerov M I and Andreev G N 2001 *Vib. Spectrosc.* **25** 177
[29] Bruker Optik GmbH 2002 *OPUS* Version 4.0 Germany
[30] Berg R W 1996 *Proc. 17th Riso Int. Symp. on Mater. Sci: High Temp. Electrochem, Ceram. and Metals* ed F W Poulsen, N Bonanos, S Linderoth, M Mogensen and B Z Christiansen (Roskilde: Riso Nat. Lab.) p 175
[31] Tai L W, Nasrallah M M, Anderson H U, Sparlin D M and Sehlin S R 1995 *Solid State Ion.* **76** 273
[32] Huang K, Lee H Y and Goodenough J B 1998 *J. Electrochem. Soc.* **145** 3220
[33] Iliev M N, Abrashev M V, Lee H G, Popov V N, Sun Y Y, Tomsen C, Meng R L and Chu C W 1998 *Phys. Rev.* B **57** 2872
[34] Livage J, Henry M and Sanchez C 1988 *Prog. Solid State Chem.* **18** 259
[35] Huang K and Goodenough J B 1998 *J. Solid State Chem.* **136** 274
[36] Petrykin V and Kakihana M 2005 *Handbook of Sol–Gel Science and Technology: Processing Characterization and Applications* vol 1, ed H Kozuka (Boston, MA: Kluwer Academic) pp 77–103
[37] Kahoul A, Nkeng P, Hammouche A, Naamoune F and Poillerat G 2001 *J. Solid State Chem.* **161** 379
[38] Li X, Agarwal V, Liu M and Rees W S Jr 2000 *J. Mater. Res.* **15** 2393
[39] Laberty-Robert Ch, Ansart F, Deloget C, Gaudon M and Rousset A 2001 *Mater. Res. Bull.* **36** 2083
[40] Iliev M N, Abrashev M V, Laverdiere J, Jandl S, Gospodinov M M, Wang Y Q and Sun Y Y 2006 *Phys. Rev.* B **73** 64302
[41] Fedorov I, Lorenzana J, Dore P, Marzi G De, Maselli P, Calvani P, Cheong S W, Koval S and Migoni R 1999 *Phys. Rev.* B **60** 11875
[42] Martin-Carron L, Andres A De, Martinez-Lope M J, Casais M T and Alonso J A 2002 *Phys. Rev.* B **66** 174303
[43] Mayr F, Hartinger Ch and Loidl A 2005 *Phys. Rev.* B **72** 024425
[44] Kuznetsova T, Sadykov V, Batuev L, Moroz E, Burgina E, Rogov V, Kurina L and Neophytides S 2005 *React. Kinet. Catal. Lett.* **86** 249
[45] Stoilova D, Georgiev M and Marrinova D 2005 *J. Mol. Struct.* **738** 211
[46] Scholes F H, Furman S A, Hughes A E, Nikpour T, Wright N, Curtis P R, Macrae C M, Intem S and Hill A J 2006 *Prog. Organ. Coatings* **56** 23